Supplementary Information:

Observation of large spontaneous emission rate enhancement of quantum dots in a broken-symmetry slow-light waveguide

Hamidreza Siampour,[1,§,*] Christopher O'Rourke,[1] Alistair J. Brash,[1] Maxim N. Makhonin,[1] René Dost,[1] Dominic J. Hallett,[1] Edmund Clarke,[2] Pallavi K. Patil,[2] Maurice S. Skolnick,[1] A. Mark Fox[1]

[1] Department of Physics and Astronomy, University of Sheffield, Hicks Building, Sheffield S3 7RH, UK

[2] EPSRC National Epitaxy Facility, Department of Electronic and Electrical Engineering, University of Sheffield, Sheffield S1 3JD, UK

[§] Current address: Cavendish Laboratory, University of Cambridge, J. J. Thomson Avenue, Cambridge CB3 0HE, UK

[*] Email: hs807@cam.ac.uk

Section A: Design of the glide-plane photonic crystal waveguide

The glide-plane photonic crystal waveguide (PCW) was designed by using two parallel W1-PCWs and continuously reducing their centre-to-centre distance while simulating the corresponding band structure, as shown in Figure S1.We start with the band structure of a single W1 waveguide as shown in Figure S1a and S1d. We then move to two W1-PCWs that were displaced laterally by half a period to obtain glide-plane symmetry, as shown in Figures S1b and S1e. In the final design the two W1 waveguides merge to form the glide-plane waveguide, as shown in Figures S1c and S1f. In this case the two bands meet at the zone edge giving no band gap for the slow light. The design thus gives a broadened slow-light region near the band edge without a band gap.

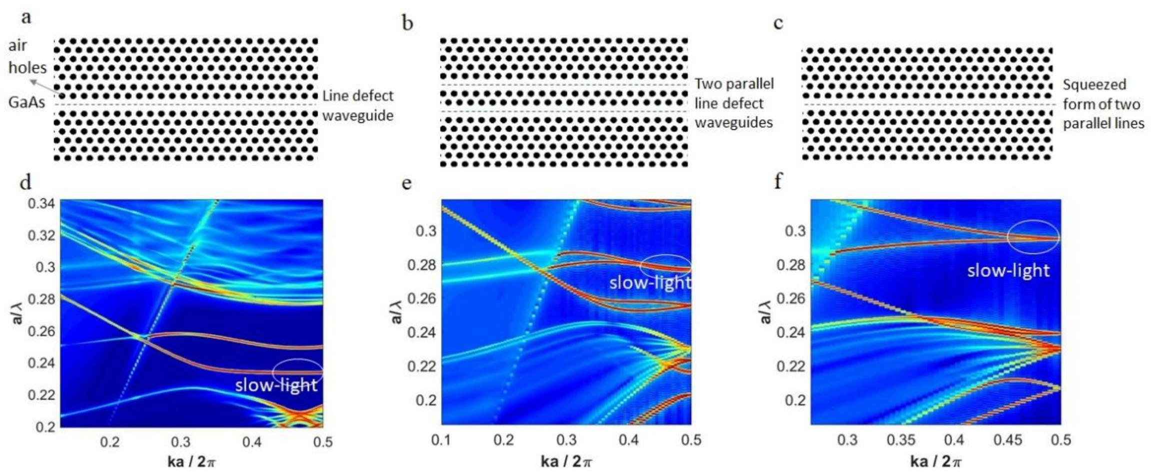

Figure S1: Design of the glide-place line defect waveguide. (a) Line defect waveguide in a triangular lattice of air holes with up-down symmetry, i.e., a W1 waveguide. (b) Two parallel W1 waveguides. (c) Line defect waveguide with an up-down glide-plane symmetry. The glide-symmetric waveguide is formed by reducing the distance between two parallel W1 waveguides until they become one line defect waveguide. (d-f) Simulated band structures of the photonic crystal waveguides shown in (a-c): (d) W1 waveguide; (e) two parallel W1 waveguides; (f) glide-symmetric waveguide. The radii of the nanoholes are 30% of the lattice constant.

Figures S2, S3 and S4 discuss the design of a device with a slow-light region at 916 nm. The actual devices that were studied had a range of slow-light band edges, but the design strategy follows the same methodology as discussed here.

It is important that the device should have single-mode operation in the slow-light glide-symmetric waveguide. This was achieved by further modification to the size of the nanoholes and their vertical displacement following a theoretical design performed by S. Mahmoodian et. al[1,2] as shown in Figure S2(a). Figure S2(b) shows the dispersions properties of the waveguide modes and the slow-light region near the crossing point. The dispersion curve has only a single mode in the slow-light region. Figure S2(c) presents the waveguide coupling efficiency, i.e. the β-factor, for the 20 different positions of a dipole emitter shown in the inset. For the optimized design with a slow-light band edge at around 916 nm, we calculated a near unity coupling efficiency in the slow-light region, as shown by the red data points in Figure S2(c). However, for the same positions with a wavelength far from the slow light region, the β-factor varies much more strongly with position, as shown by the black data points.

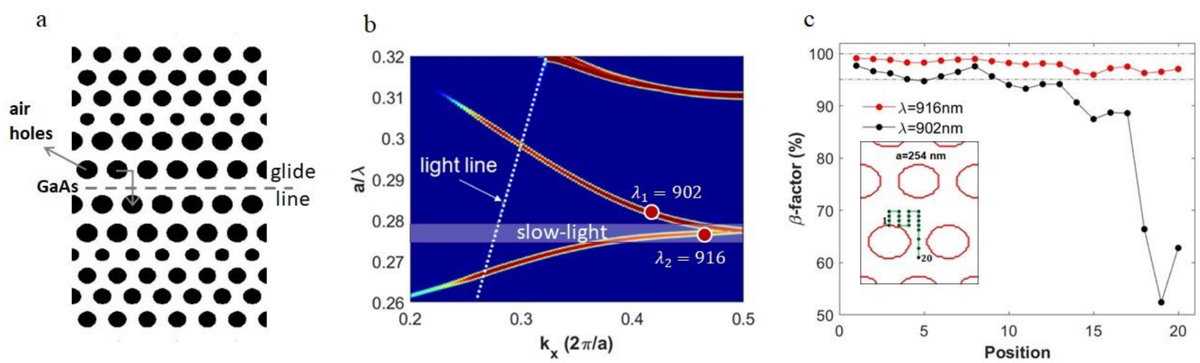

Figure S2: Characteristics of the photonic crystal waveguide (PCW) mode. (a) Glide-symmetric waveguide with modified nanohole sizes and their vertical displacements. (b) Simulated band structure of the optimised PCW shows dispersions properties of the waveguide modes and the slow-light region near the crossing point. (c) Simulated emitter-waveguide coupling efficiency, i.e. β-factor, for various positions of the embedded QDs. For the QDs emitting in the slow light region of the waveguide near the band edge, (red dots with a/λ=0.277 where a=254 nm and λ=916 nm), a near-unity β-factor is achievable that is almost position independent. For the QDs outside the slow-light region (black dots with a/λ=0.282), the β-factor is highly position dependent.

In the slow-light region near the crossing point, the insertion loss becomes very large due to the large group index ($n_g \rightarrow \infty$). In order to make a smoother transition (and therefore lower insertion loss) from the slow-light glide-plane waveguide (GPW) to the rest of photonic circuitry, we designed a slow-to-fast light adapting coupler (Figure S3). The device has three sections as shown in Figure S3a. Section #1 at the centre is the glide-plane waveguide (GPW). Section #2 on both sides of the GPW is a fast-light section that reduces the reflection losses at the end of the GPW. This is done by moving from point #1 to #2 on the GPW dispersion by varying the lattice constant, as shown in Figure S3b. Finally, Section #3 is a glide-plane nanobeam (GPN) that smoothly couples to a standard nanobeam and hence to the rest of the photonic circuit. The GPN is designed with the bottom of its band edge aligning with the fast light GPW, as shown in Figure S3c. The results in Figure S3b give the coupling between a source positioned within section #1 and the central slow-light GPW. The adaptor design ensures that these photons can then be coupled efficiently out of the central region to the rest of the photonic circuit. There is no cut off for the GPW but there is one for the GPN. This allows experimental verification of the design that is used to determine the position of the slow light region. Refer to Section C.

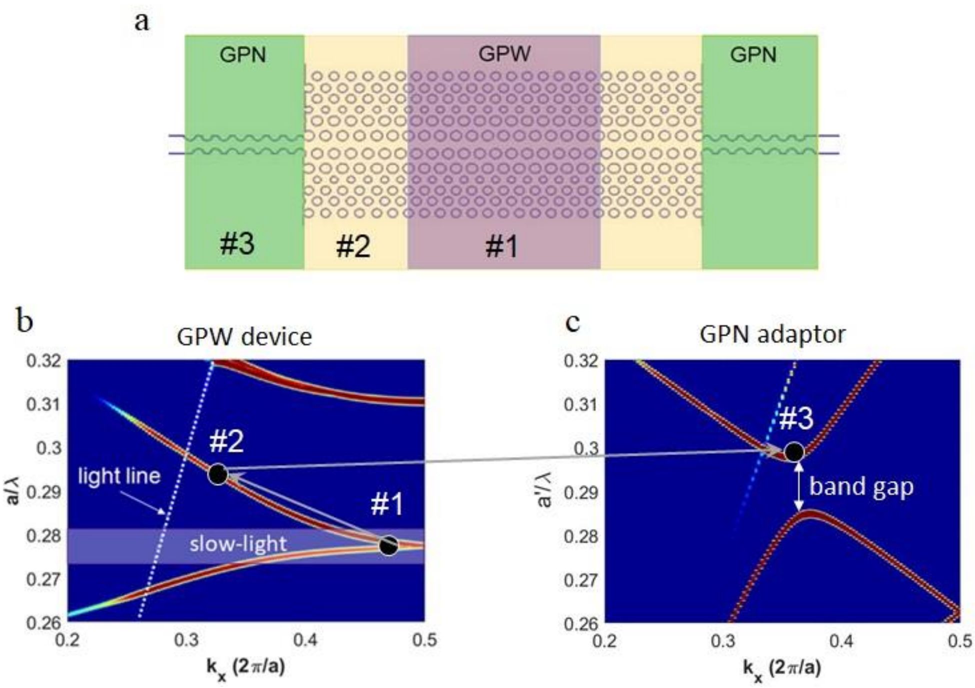

Figure S3: Schematic of the device layout and the design rationale for the slow-to-fast light coupler. (a) Device layout containing GPW in the central section (section #1), and the waveguide adapting sections (#2 and #3) for slow-to-fast light coupling. (b, c) Simulated band structure of the GPW (b) and GPN (section #3, c). The GPW structure in section #2 has a 7% expanded lattice constant in comparison with the GPW in the section #1 which allows operating at a point on the dispersion diagram with higher slope (lower group velocity) in section #2. The section #3 is a nanobeam waveguide modulated with the first rows of the GPW nanoholes (GPN) and served as an intermediate section between a standard nanobeam and the GPW sections.

Dispersion analysis enabled us to improve the optical waveguide adaptor design and thereby achieve insertion factors up to 88% for a source positioned near the middle of section #1 and operating near the crossing point of the slow-light region. Figure S4 shows FDTD simulations (Lumerical software) for the device considered in Figures S2 and S3. The top panel shows the field profile at 916 nm, while the bottom panel shows the variation of the coupling factor on tuning away from the slow-light region. Our design enables the highest coupling factor to be obtained for the source emitting at the slow-light band edge.

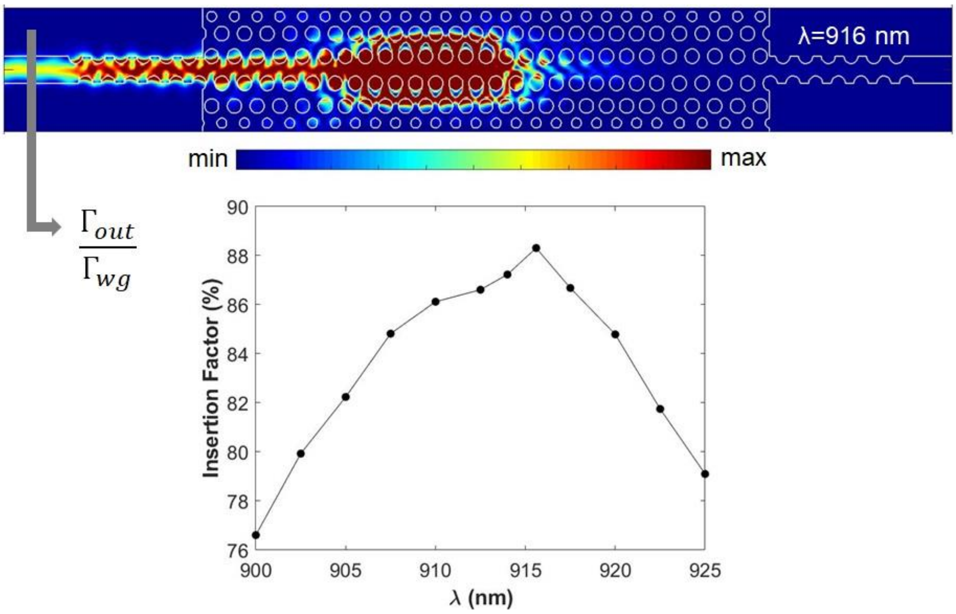

Figure S4: Simulated waveguide transmission from slow to fast-light sections of the photonic crystal device with the design shown in Figure S3. Top panel: Simulated waveguide mode at λ=916 nm. Bottom panel: Wavelength dependence of the slow-to-fast light transmission efficiency, i.e. Γ_{out}/Γ_{wg}(insertion factor).

Section B: Optical measurements

Figure S5 shows a schematic of the optical setup and the cryogenic system.

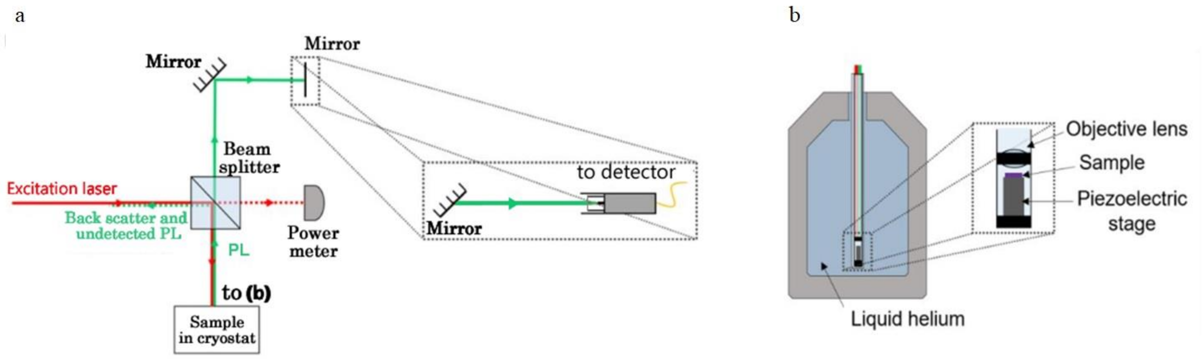

Figure S5: A schematic of the optical setup and cryostat. (a) Confocal setup. (b) Liquid helium cryostat.

Section C: Experimental determination of the slow-light region

The wavelength of the slow-light region was determined by combining transmission measurements with band-structure simulations. Quantum dots excited near one of the outcouplers were used as an internal light source and the transmission spectrum was obtained by measuring the spectrum at the opposite outcoupler, as shown in Figures S6a and S7a. The observed spectrum is the convolution of the broad quantum-dot ensemble emission and the transmission of the waveguide. The measured spectrum shows a clear cut-off at the long-wavelength end. The slow-light region in the GPW does not have a cut-off as there is no band gap, and the wavelength of the cut-off is determined instead by the GPN adaptor band gap. Hence the wavelength of the cut-off fixes a clear point on the GPN band structure for the actual device under investigation.

In the simulations we assume that the hole diameters and lattice periodicity vary from the design parameters by a scaling factor that is consistent for the particular device under test. We simulate the band structure of the GPN and find the parameters that give the observed long-wavelength cut-off. This enables the determination of the actual parameters for the GPW, and hence its band structure. Examples of how this is done for two different devices are presented in Figures S6 and S7.

Figure S6b shows the transmission spectrum obtained for device #1, which is the one used for the chiral quantum dot results presented in Figure 4 in the main text. The long-wavelength cut-off is observed at 880 nm. The GPN band structure that matches this cut-off is shown in the lower panel of Figure S6c. By applying the same scaling parameter, we deduce the band structure of the GPW shown in the top panel of Figure S6c, and hence that the slow-light band edge occurs at 877.4 nm. Figures S7b and S7c show equivalent results for device #10 which has a cut-off at 939 nm and a slow-light region occuring at 937 nm. Chirality results are presented for this device in Figure S8.

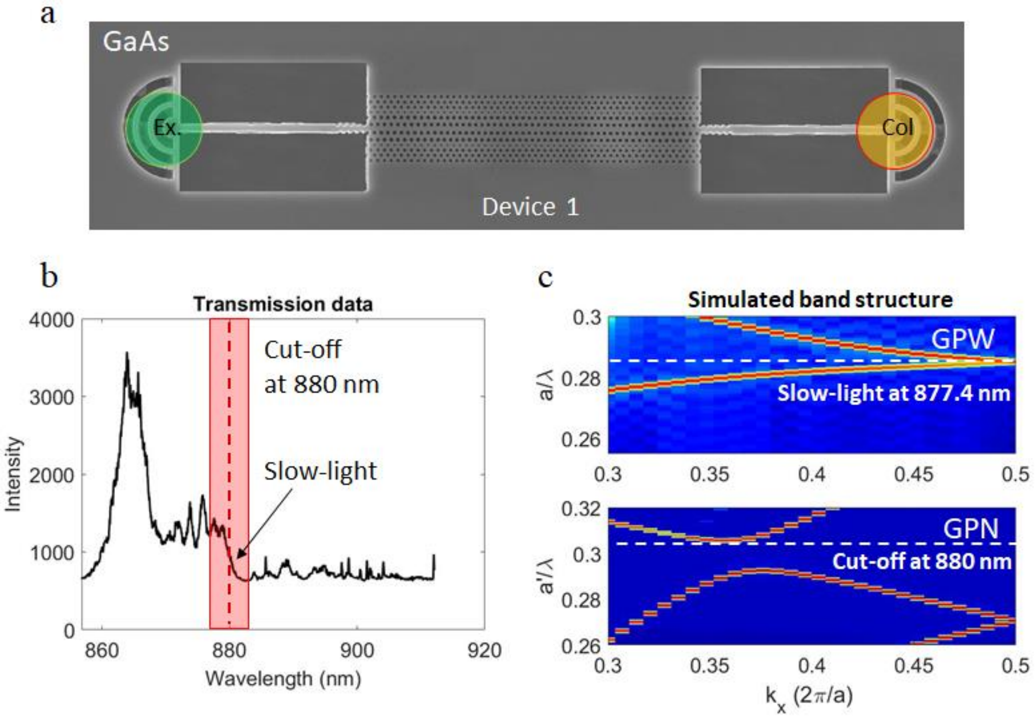

Figure S6: (a) SEM image of Device #1 with lattice constant of a= 250 nm for the slow-light section and extended lattice constant of a′ = 1.07a for the adaptor. (b) High power photoluminescence transmission measurement data where one end is excited with an 808 nm laser and the photons collected from the other end are analysed using a spectrometer. (c) Simulated band structure for the glide-plane waveguide GPW (top), and glide-plane nanobeam (GPN), respectively.

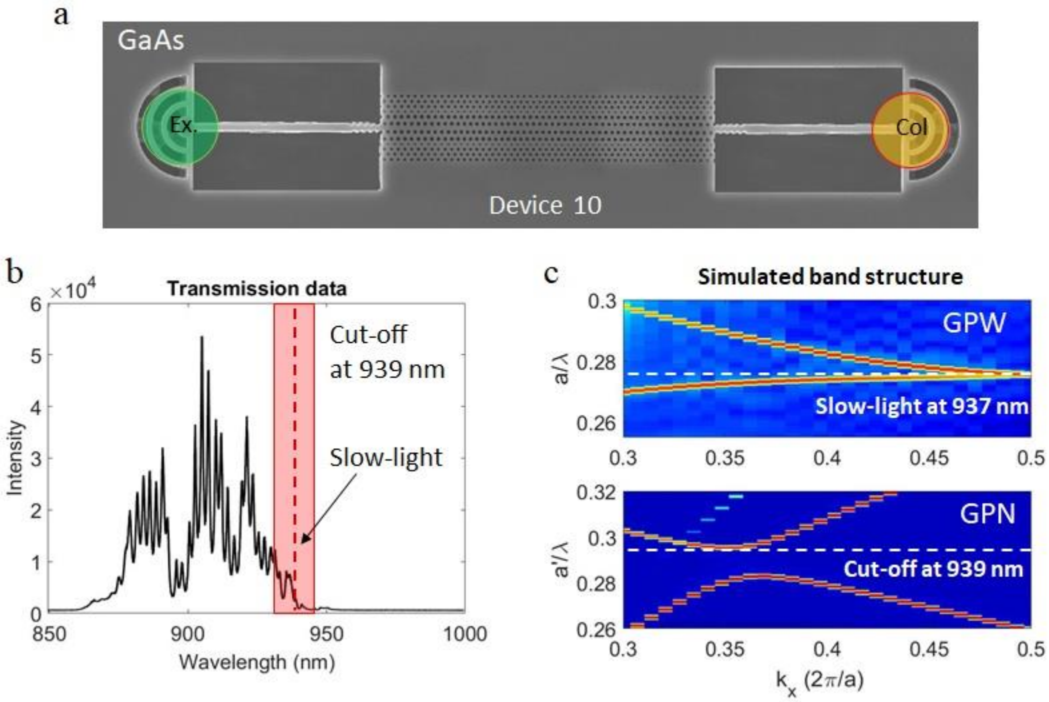

Figure S7: (a) SEM image of Device #10 with lattice constant of a= 258 nm for the slow-light section and extended lattice constant of a′ = 1.07a for the adaptor. (b) High power photoluminescence transmission measurement data where one end is excited with a 808 nm laser and the photons collected from the other end are analysed using spectrum analyser. (c) Simulated band structure for the glide-plane waveguide GPW (top), and glide-plane nanobeam (GPN) adaptor, respectively.

Section D: Chirality measurements

Figure S8 shows quantum optical measurements of chirality for a typical GPW system with all the dots showing strong chiral emission, which confirms the fact that the glide plane waveguides give large chiral regions. Also, opposite chiralities are observed for different dots, as expected for randomly positioned dots.

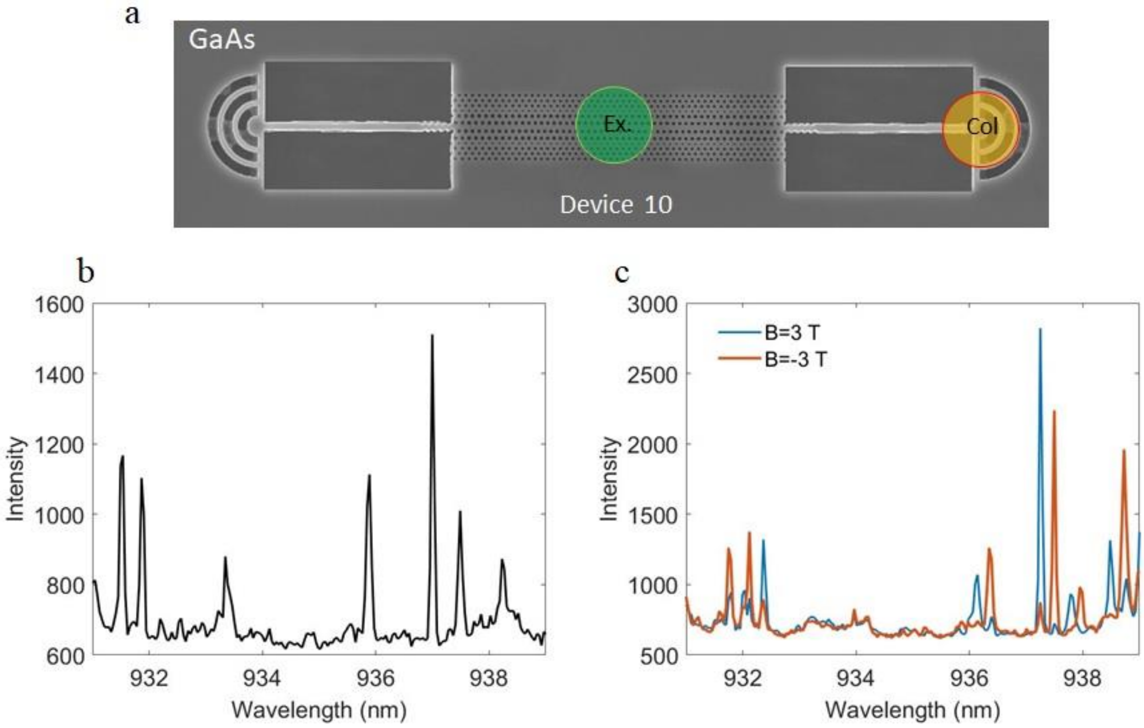

Figure S8: Quantum optical measurements of chirality. (a) SEM image of the device. (b) Photoluminescence spectra when the non-resonant laser (808 nm) excited embedded quantum dots at the centre of the device and photons are collected from the outcoupler end. (c) Chiral measurements. Strong chirality was observed for a series of dots.

Section E: Hanbury Brown Twiss measurements

Figure S9 shows the results of Hanbury Brown-Twiss (HBT) measurements performed on the fast non-chiral quantum dot considered in Figure 2 of the main text. The results were performed under continuous wave non-resonant excitation, where the Purcell factor is given by the red data points in Figure 2d of the main text.

Figure S9a shows the HBT results obtained with the dot emitting at 911.2 nm where the QD lifetime is 100 ps, corresponding to a Purcell factor of 12 (See main text Figure 2d). The convolved response time of the two superconducting nanowire detectors used for these measurements was 114 ps. Since this is longer than the QD lifetime, the raw anti-bunching dip with a minimum of 0.60 does not give a true measurement of the photon statistics. The red curve shows the deconvolved result with a dip dropping well below 0.5, confirming the single-photon nature of the source.

Figure S9b shows the electrical tuning curve of the QD, and Figure S9c presents HBT results for an applied voltage of 1.59V where the emission wavelength is > 912 nm. The QD is further away from the slow-light band edge and has a longer lifetime of ~200 ps. The raw data shows a dip going down to 0.16 without any detector deconvolution.

The variation of the depth of the antibunching dip is an independent measurement of the variation of the emission time of the QD with detuning from the slow-light band edge. The fact that the raw antibunching dip increases from 0.16 to 0.60 by tuning to the band edge confirms that the QD lifetime is shorter than the detector response time.

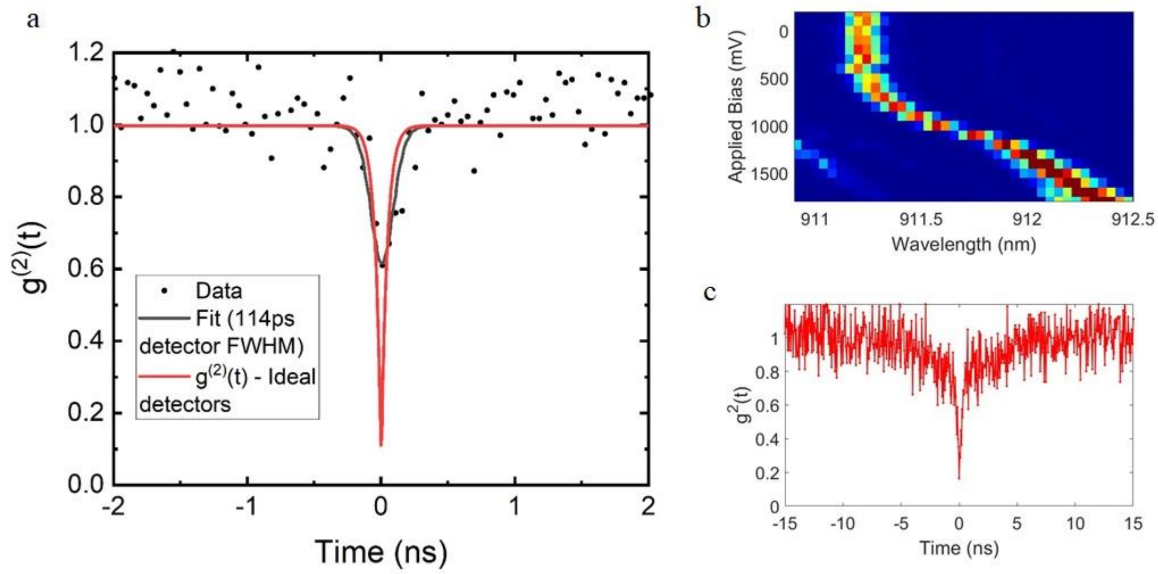

Figure S9: HBT measurements. (a) The second-order auto-correlation measurement for emission from the QD coupled to the slow-light waveguide shown in Figure 2 in the main text. The red curve is a deconvolved fit based on a 114 ps detector response time. The result confirms the single photon nature of emission due to the strong antibunching dip ($g^2(0) = 0.11$). (b) The photo-luminescence scan for the QD versus applied voltage. (c) HBT measurements for a dot slightly detuned from the band edge (1.59 V bias, at λ=912 nm) where the lifetime is ~200ps. The result indicates a raw antibunching dip with $g^2(0) = 0.16$ without any detector response deconvolution.

Reference

1 Mahmoodian, S., Prindal-Nielsen, K., Söllner, I., Stobbe, S. & Lodahl, P. Engineering chiral light-matter interaction in photonic crystal waveguides with slow light. *Opt. Mater. Express* **7**, 43-51, doi:10.1364/OME.7.000043 (2017).

2 Østfeldt, F. T. *et al.* On-Demand Source of Dual-Rail Photon Pairs Based on Chiral Interaction in a Nanophotonic Waveguide. *PRX Quantum* **3**, 020363, doi:10.1103/PRXQuantum.3.020363 (2022).